Green Chemistry

PAPER

View Article Online
View Journal

Cite this: DOI: 10.1039/d5gc06974b

Influence of the cathodic binder on CO_2 electroreduction to formic acid in a three-compartment electrolyzer

Konstantin von Foerster, *[a,b] Sergio Sanz, *[a] Krzysztof Dzięcioł,[a] Urbain Nzotcha,[a] Bastian Rutjens,[a,b] Bernhard Schmid,[a] Hermann Tempel[a] and Rüdiger-A. Eichel[a,b]

Restructuring synthetic processes is essential to enable decarbonization in industrial synthesis. The electrochemical reduction reaction of CO_2 to value-added products, such as formic acid, integrates CO_2 as a feedstock and can be coupled with renewable energy sources to enable a CO_2-negative synthetic process. Techno-economic analyses (TEAs) present the direct formic acid production (DFAP) reactor as the most promising design for industrial competitiveness. Using this electrolyzer design, we fabricated custom-made cathodic Bi_2O_3-based gas diffusion electrodes (GDEs) with various ionomer materials and evaluated the performance of the reactor. Contrary to our initial expectations, the anionic polymer (PiperION) used as a binder exhibited low performance at higher current densities (350 and 500 mA cm^{-2}) when paired with its corresponding anion exchange membrane (AEM), suggesting that achieving a homogeneous GDE/AEM interface may not be as critical as previously thought. Akin to the anionic binders, the cationic ionomer (Nafion) exhibited good performance only at 200 mA cm^{-2}. The best performance was obtained with the non-ionic polymer (PVDF/HFP), achieving the highest reported current density (750 mA cm^{-2}) with this electrolyzer design while maintaining stable operation with high faradaic efficiency (69%), high formic acid concentrations (3.8 M; ~16 wt%), and an optimized energy consumption of 8.3 kWh kg^{-1}. We postulate that the higher hydrophobicity of PVDF/HFP suppresses water accumulation within the catalyst layer, thereby enhancing CO_2 diffusion and supporting higher current densities, while reducing diffusion overpotentials. Scanning electron microscopy (SEM) and X-ray computed tomography (XCT) helped to identify the migration of potassium and bismuth within the cathode. TEA studies indicate promising scalability potential based on the experimental data presented in this study, driven by the ability to produce high concentrations of formic acid at high current densities.

Received 23rd December 2025,
Accepted 13th April 2026

DOI: 10.1039/d5gc06974b

rsc.li/greenchem

Green foundation

1. The electrochemical reduction of CO_2 to formic acid integrates CO_2 as a feedstock, enabling a CO_2-negative synthetic process. Our endeavor toward the production of "green" formic acid focuses on the development of cathodic electrodes that promote high selectivity and productivity.
2. Investigating the use of different ionomers in Bi_2O_3-based gas diffusion electrodes (GDEs) revealed significant variations in key performance indicators. The PVDF/HFP ionomer achieved the highest reported current density (750 mA cm^{-2}) to date with the direct formic acid electrolyzer design. Techno-economic analyses indicate promising scalability potential based on the experimental data presented in this study.
3. The results obtained in this work provide an optimized electrode design and insights into the structural changes in the GDEs corresponding to a cell active area of 5 cm^2. To advance toward applicability, economies of scale must be implemented.

Introduction

Renewable electricity generation plays a key role in reducing CO_2 emissions and decreasing the dependency on fossil fuels at comparatively low cost,[1,2] but its intermittent nature poses challenges for maintaining a consistent energy supply. Power-to-X technologies transform surplus renewable energy into fuels and chemicals that can be stored or converted back into energy during

[a]Institute of Energy Technologies – Fundamental Electrochemistry (IET-1), Forschungszentrum Jülich, Jülich, Germany. E-mail: s.calvo@fz-juelich
[b]Institute of Physical Chemistry, RWTH Aachen University, Aachen, Germany. E-mail: konstantin.foerster@rwth-aachen.de

periods of low renewable energy production. Herein, the electrochemical reduction of CO_2 (eCO_2R) to value-added chemicals presents a promising route for decarbonizing existing synthetic processes.[3] Specifically, the eCO_2R to CO,[4] formic acid (HCOOH),[5] ethylene,[6] and ethanol have been intensively studied due to the industrial relevance of these products.

The eCO_2R-to-HCOOH is especially promising, as technological developments bring it closer to economic competitiveness with the conventional energy-intensive process that contributes significantly to CO_2 emissions.[7–9] It can be performed under alkaline conditions as CO_2-to-formate conversion, while actual eCO_2R-to-HCOOH is possible under acidic conditions or *via* direct formic acid production (DFAP), which only employs deionized water as a liquid electrolyte. The DFAP electrolyzer features a three-compartment design[10] (Fig. 1) that enables the production of pure HCOOH (free of liquid electrolyte), thanks to the presence of a porous ion exchange resin (*e.g.*, Amberlite IR-120H) in the center compartment, which facilitates proton conduction and provides structural stability.[11] The center compartment is separated from the cathode and anode by an anion exchange membrane (AEM) and a cation exchange membrane (CEM), respectively. The AEM establishes an alkaline environment around the catalyst layer—fundamental for an efficient eCO_2R—and allows the transport of formate anions into the center compartment, where they recombine with anodic protons generated by the oxygen evolution reaction (OER) to produce HCOOH. Technoeconomic analysis highlights the DFAP electrolyzer as the most promising design to compete with the established industrial production of HCOOH when economies of scale are considered. However, technological advances in key DFAP cell components (particularly with ion exchange membranes, gas diffusion electrodes, and solid-state electrolyte) are still required with laboratory prototypes before considering the implementation of higher electrode active areas and multiple-cell stacking.[12]

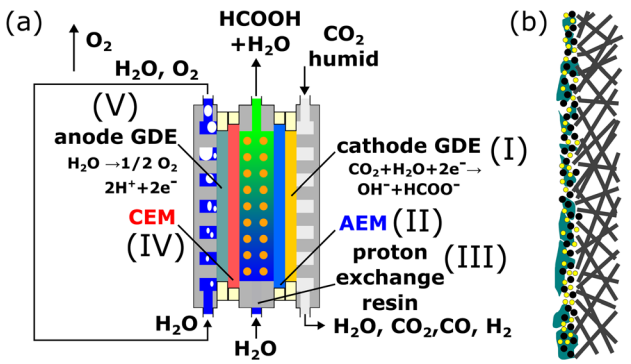

Fig. 1 (a) Schematic representation of the employed DFAP electrolyzer (Fig. S1 includes periphery). (I) Cathode GDE, fed with humidified CO_2. (II) Anion exchange membrane (AEM). (III) Center compartment, filled with a proton exchange resin, and water-fed in a single pass mode. (IV) Cation exchange membrane (CEM). (V) Anode GDE, water-fed in recirculation mode. (b) Schematic view of the cathode architecture, featuring a gas diffusion layer (GDL) substrate (dark grey) and a catalyst layer consisting of catalyst (yellow), conductive carbon black (black), and polymer binder (green).

As developer of the DFAP design, Dioxide Materials recommended the use of Sustainion AEM and its related ionomer in the cathodic GDE. It was proposed that the imidazolium moiety interacts with CO_2, reducing the free energy barrier required for the reduction reaction.[13,14] A more recent report demonstrated comparable results using the PiperION AEM (featuring a piperidinium moiety as the ionic exchange site), supporting its viability as an alternative to the Sustainion AEM.[15] A typical cathodic GDE consists of a catalyst layer (CL) comprising catalyst particles, conductive carbon, and ionomer. The CL is supported on a gas diffusion layer (GDL), which is a conductive and porous material.[13,15] To ensure a homogeneous GDE/AEM interface and the required transport of formate, carbonate, and bicarbonate across the membrane, the ionomer used in the CL tends to be the same polymer as the AEM. However, given the multiple functional nature of the ionomer in the CL—including ion conduction, reaction site formation, mechanical cohesion, water management, and layer stability—exploring the use of ionomers different from the AEM type may offer performance benefits.

To address this gap, we investigated how different ionomers in the cathodic GDE design (based on Bi_2O_3 nanoparticles) influence the electrochemical performance of the DFAP electrolyzer. Specifically, we compared cationic (Nafion), anionic (Sustainion and PiperION), and non-ionic (poly-vinylidene difluoride/hexafluoropropylene copolymer, PVDF/HFP) ionomers, evaluating their compatibility when paired with PiperION AEM. Experimental data obtained using the PiperION binder were previously published by us[15] and are used here for comparison with the other ionomers investigated. Furthermore, using scanning electron microscopy (SEM) and X-ray computed tomography (XCT), we aimed to identify the migration of potassium and bismuth within the cathode to better understand their impact on the cell performance.[13,15,16–18]

Experimental section

Cathode fabrication

A catalyst ink consisting of 100 mg of Bi_2O_3 (Sigma-Aldrich, 99.9%, <100 nm), 100.0 mg of Vulcan-72XC (Cabot), and 6.25 mg (25 mg in case of PVDF/HFP) of a polymeric binder from a dispersion (Sustainion XA-9, Dioxide Materials; Nafion 20%, Ion Power; PVDF/HFP copolymer 1 : 0.37, Sigma-Aldrich, 5% in acetone), and 5 mL of ethanol (acetone for PVDF/HFP binder) was homogenized in an ultrasonic bath for approximately 30 min. Subsequently, the mixture was spray-coated onto 2.5 × 2.5 cm^2 of carbon paper (Toray TGP-H-120 with 30 wt% PTFE, Quintech) *via* a handheld airbrush (Tamiya Spray-Work HG, 0.3 mm). Ionomer loadings using the PVDF/HFP binder in the range of 6.25–125 mg were investigated. An optimal load of 25 mg was identified. In contrast, for the other binders, 6.25 mg provided the best compromise, as higher loading decreased selectivity and increased the cell potential (Fig. S2). This lower loading for ionomer binders was also employed by Dioxide Materials.[19]

Electrolyzer operation

The three-compartment DFAP electrolyzer (Dioxide Materials) comprised an IrO_2-based GDE anode (Dioxide Materials), a Nafion N324 cation exchange membrane (CEM, Ion Power), an Amberlite IR-120H cation exchange resin (Acros Organics), a PiperION-A40-HCO3 (PiperION AEM, Versogen) anion exchange membrane (AEM), and a self-fabricated Bi_2O_3-based GDE cathode. Carbon dioxide gas (99.995%, Air Products) was humidified with a humidifier (Nafion-based permeable membrane, Perma Pure) and fed in excess (60–225 sccm, λ = 8) to the cathode compartment. Gaseous products emerging from the cathode compartment outlet were analyzed using in-line gas chromatography (GC; Trace 1310, Thermo Fisher), with injections at ~6 min intervals and the volume quantified with a drum gas counter (TG0.5-PP-PP, Ritter). A PGSTAT302N potentiostat (Metrohm) was used as a power supply and for the electrochemical measurements. A peristaltic pump (Masterflex Reglo Miniflex Digital Pump, Ismatec) was employed for recirculation of the deionized water (~0.055 mS cm^{-1}) as anolyte at 3 mL min^{-1}. Two syringe pumps (LA-100, Landgraf Laborsysteme) supplied the center compartment with deionized water at 0.1 mL min^{-1} in single-pass mode. The product was collected from the center compartment and analyzed by off-line ion exclusion chromatography (S155, Sykam, Germany). GC analysis used two channels to quantify the gas products: one with a 2 m × 1 mm column packed with 5 Å molecular sieves and Ar as carrier gas for quantifying H_2, and another with a 3 m × 1 mm ShinCarbon ST column and He as carrier gas for measuring CO and atmospheric gases. Both channels employed thermal conductivity detectors.

Electrochemical measurements

For every experiment, a newly fabricated cathodic GDE and an AEM were employed. The PiperION AEM was immersed in a 1 M KOH solution for 10 hours and rinsed with deionized water before use. After cell assembly, the center compartment was flushed with 0.5 M of K_2SO_4 solution for 20 seconds (2–3 mL) to increase the initial conductivity. To ensure stable operation of the electrolyzer, chronoamperometry (CA) at 5 V was performed until the cell current stabilized between 2.0 and 3.5 A. The first block of measurements assessed the performance stability of the electrolyzer using chronopotentiometry (CP) at 200 mA cm^{-2} for 3 h. Subsequently, the second block of experiments investigated the effect of current density on the electrolyzer's performance using CP at 500, 350, and 200 mA cm^{-2} (initially starting at 750 mA cm^{-2} for specific cathodic GDE configurations). In the stability measurements at 200 mA cm^{-2}, liquid samples were collected hourly, while one 30 minute sampling was obtained at each subsequently applied current density after equilibration of the cell potential. In-line GC measurements were performed continuously at intervals of approximately 380 s.

Contact angle measurements

The contact angle of sessile drops on pristine and post-mortem GDEs was determined using an optical contact angle goniometer (OCA100, DataPhysics Instruments, Germany). For each sample, sessile drops of 2 μL of deionized water were imaged at three different positions on each GDE.

SEM imaging

To examine morphology, top, and cross-sectional views, SEM images of pristine and used GDEs were obtained. An FEI Quanta 650 scanning electron microscope (SEM) with an acceleration voltage of 10 kV was used for secondary electron and backscattered electron imaging. EDX mapping was performed with an Octane Elite EDX detector with a 10 kV acceleration voltage.

X-ray computed tomography

X-ray computed tomography (XCT) measurements were performed on a Zeiss Xradia 620 Versa at resolutions of 3.4 μm and 0.68 μm (voxel size, see Table S2 for further details). An arrow-shaped post-mortem GDE and an AEM sample with dimensions of approximately 4 mm × 25 mm were measured. To prevent AEM damage during dry-out, the AEM sample was immersed in 0.5 M $KHCO_3$ solution for two hours and rinsed with deionized water to perform an anion exchange with bicarbonate. The samples were measured in a dry state.

Key performance indicators

Electrolyzer performance was evaluated using experimental data from the electrochemical experiments in combination with the concentrations obtained by IC and GC measurements, using the following key performance indicators: faradaic efficiency of formic acid (FE_{FA}, eqn (1)), faradaic efficiency of carbon monoxide and hydrogen (FE_{CO} and FE_{H_2}, eqn (2)), and the energy consumption of formic acid (Q_{FA}, eqn (3)).

$$FE_{FA} = 100\% \times \frac{cVzF}{jA\Delta t} \quad (1)$$

$$FE_{CO/H_2} = 100\% \times \frac{p\dot{V}zF}{RTjA} \quad (2)$$

$$Q_{FA} = \frac{UjA\Delta t}{cVM} \quad (3)$$

Here, c denotes the concentration of formic acid, V the liquid sample volume, z the stoichiometric number of electrons required to form the product, F the Faraday's constant, j the current density, A the cathodic electrode area, Δt the sample collection time interval, p the pressure, $\dot{V}$ the gas volume flow rate in the time interval, R the gas constant, T the temperature, U the cell voltage, and M the molar mass of formic acid.

Results and discussion

Influence of the cathodic GDE binder on the electrolytic performance using PiperION AEM

To ascertain the influence of the binder used in the self-fabricated cathodic Bi_2O_3-based electrode (see Experimental section for details) on the electrochemical performance of the reactor operating with a 40 μm PiperION AEM, chronopoten-

tiometry (CP) was initially conducted at 200 mA cm^{-2} for 3 hours. During these experiments, CO_2 humidified was supplied at 60 sccm, distilled water flowed through the anode at 3 mL min^{-1} in recirculation and in the center compartment at 0.1 mL min^{-1} in single-pass mode. Both liquid flows were previously optimized in our investigations[15] with this reactor design, yielding favorable product concentrations without affecting FE_{FA}. The anodic electrode was fixed to a commercial IrO_2-based GDE to catalyze the OER. At 200 mA cm^{-2}, the DFAP reactor operated stably with the four investigated binders (Sustainion, PVDF/HFP, and Nafion), achieving faradaic efficiencies of formic acid (FE_{FA}) ranging from 65 to 75% and cell voltages between 3.4 and 3.9 V (Fig. 2a). The best cell performance was obtained with the PVDF/HFP binder, with an energy consumption value of ~5.7 kWh kg^{-1} (Fig. 2c) and displaying the lowest standard deviation (SD) among the investigated KPIs (Fig. 2a and c). Using ionic binders (Sustainion and Nafion), the cell exhibited lower reproducibility, as indicated by the higher SD (Fig. 2a and c and Table S1). Hydrogen evolution represents the primary competing reaction for all binders, whereas the FE_{CO} is consistently below 5%.

Subsequently, a series of experiments investigated the impact of the binder on the electrochemical performance across a range of current densities (750, 500, 350, and 200 mA cm^{-2}; 750 mA cm^{-2} was only achieved at specific cathodic GDE configurations). The CO_2 gas supply was adjusted to 60,

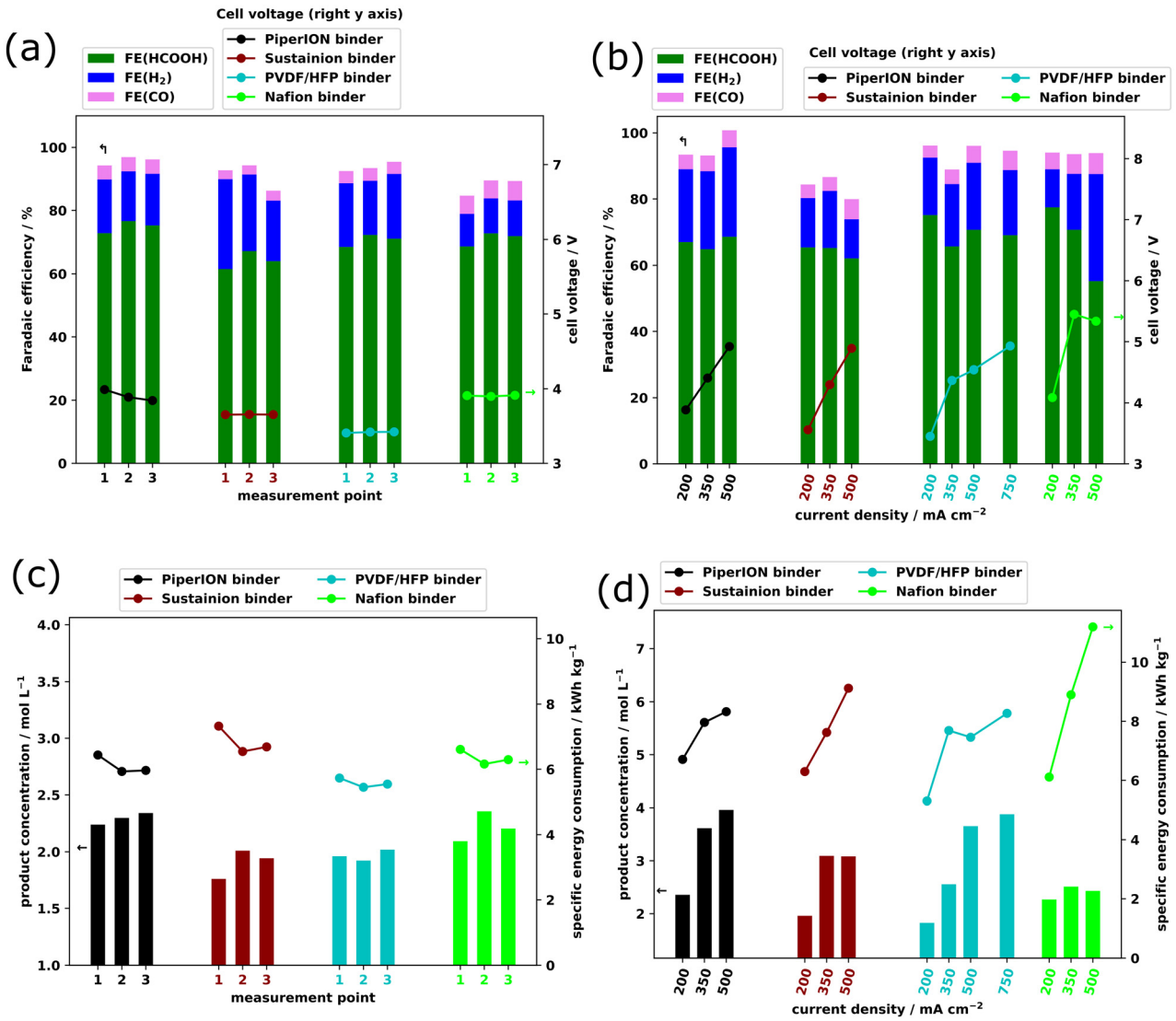

Fig. 2 Key performance indicators (KPIs) using GDEs with different binders using a 40 μm PiperION AEM: (a) faradaic efficiency and cell voltage variation over 3 h measuring time (1 h interval) at 200 mA cm^{-2}, (b) faradaic efficiency and cell voltage variation at different current densities (sampling after 30 min of stable cell operation), (c) formic acid concentration and energy consumption over 3 h measuring time (1 h interval) at 200 mA cm^{-2}, and (d) formic acid concentration and energy consumption at different current densities (sampling after 30 min of stable cell operation). Error bars in Table S1 indicate the standard deviation from two experiments. Table S1 reports detailed performance values and standard deviations. Data from plotted results using the PiperION binder were obtained from ref. 15, available under a CC-BY 4.0 license; copyright 2024 B. Rutjens *et al.*

105, 150, and 225 sscm for 200, 350, 500, and 750 mA cm^{-2}, respectively, while all other conditions were kept constant. Stable operation at current densities between 200 and 500 mA cm^{-2} was achieved across all cathodic GDE architectures, with FE_{FA} ranging from 60 to 70% (Fig. 2b). The GDE with the non-ionic PVDF/HFP binder outperformed the other materials, enabling high formic acid concentrations with low energy consumption at both 200 and 500 mA cm^{-2}, and even sustaining current densities up to 750 mA cm^{-2} (Fig. 2d). At 200 mA cm^{-2}, it achieved an optimal cell voltage of ~3.5 V, and a specific energy consumption of ~5.3 kWh kg^{-1}—surpassing the best previously reported value of 5.4 kWh kg^{-1} at this current density (Fig. 2b and d).[19] At 500 mA cm^{-2}, operation with this binder maintained an energy consumption of ~7.5 kWh kg^{-1}, also representing the lowest value reported to date.[15] Notably, this work marks the first demonstration of a DFAP electrolyzer operating efficiently at 750 mA cm^{-2}, with a FE_{FA} ~70%, and a cell voltage of ~5.0 V, yielding an energy consumption of 8.27 kWh kg^{-1} (Fig. 2b and d). The cell performance using the cationic Nafion binder was only efficient at 200 mA cm^{-2}, with significantly reduced efficiency at higher current densities due to elevated cell voltages and increased energy consumption. Other cell designs involve alkaline potassium-based electrolytes, which produce potassium formate solutions at lower concentrations,[20] resulting in extra cost in the downstream processes in view of potential industrial viability.[21] Reactors involving anodic hydrogen oxidation incur significant reactant costs, albeit operating at lower potentials.[16,18] Designs employing acidic catholyte and anodic OER allow reaching high current densities;[22] however, they operate at high energy consumption and are prone to cathodic flooding, given the direct contact to the catholyte compartment.[13,23]

These results indicate that using the same polymeric material for both the AEM and the cathodic binder to promote ion conduction and ensure a homogeneous GDE/AEM interface is not essential for achieving high electrochemical performance in the DFAP design.

This finding is particularly surprising given the several micrometers average distance between the catalyst particles and the AEM, which is owed to the mixed CL in the employed electrode design (Fig. 1b).[19] Given the enhanced performance observed with the non-ionic PVDF/HFP binder, hydrophobicity is suspected to be determinant in supporting high current densities. A hydrophobic binder can suppress liquid water accumulation within the CL, thereby enhancing CO_2 diffusion and reducing the diffusion-related overpotentials.[24,25] Contact angles of 139 ± 4° and 151 ± 4° were measured for Nafion- and PVDF/HFP-bound pristine GDEs, respectively. Given that Nafion exhibits hydrophobicity only at low relative humidities,[26] the PVDF/HFP binder is the only one expected to maintain hydrophobicity under the operating conditions.

Influence of the cell activation on the performance of the DFAP electrolyzer

In the context of CO_2 electroreduction, the influence of cations on the cathodic reaction remains an area of active investigation, with several competing theories.[27] These include their role in affecting the electrostatic environment around the catalyst layer, modulating the local electric field, and helping to stabilize reaction intermediates, such as adsorbed CO_2.[28] The DFAP electrolyzer operates with deionized water through the anode and center compartment, requiring an initial 'activation' of the cell.[19] In the experiments of Fig. 2, the AEM was pre-conditioned being used in the hydroxide form and the center compartment was initially fluxed with 0.5 M K_2SO_4 water solution for 20 seconds (2–3 mL) before performing chronoamperometry (CA) at 5 V until the cell current stabilized between 2.0 and 3.5 A (400–700 mA cm^{-2} for a 5 cm^2 electrode).

This cell activation facilitates the passage of K^+ ions across the AEM and accumulation on the catalyst layer. As a result, the electrolyzer operated stably and more efficiently during the subsequent chronopotentiometry experiments.

Given the importance of membrane activation before operation, we first investigated whether PiperION pre-conditioning with KOH is necessary. To this end, we performed a standard chronoamperometry (CA) at 5 V using an untreated PiperION AEM. During the CA, a continuous flow of 0.5 M K_2SO_4 was applied, while the CO_2 flow rate was set to 150 sccm. The liquid flow rates were kept consistent with those in previous cell activation and in the experiments shown in Fig. 2 (3 mL min^{-1} in the anode and 0.1 mL min^{-1} in the center compartment). Fig. 3a displays two experiments conducted with cathodes using Nafion and PVDF/HFP binders. Using Nafion (featuring the black line in Fig. 3a), the current density presented a steady increase over time, reaching a plateau at 3000 s and 400 mA cm^{-2}. The current density measured at 5 V closely matches the value observed during cell activation in Fig. 2 using the same binder. Hence, the presence of a high alkaline medium—due to an OH^- concentration in the PiperION membrane—contacting the Nafion binder (as part of the catalytic layer) is not a requirement for the cell activation, as observed in Fig. 3a. Due to the low total mass of approximately 6 mg of Nafion binder per GDE, only a few μmols of K^+ are required to replace H^+ *via* ion exchange (SI). Furthermore, the electrochemical production of OH^- ions in the cathode may accelerate the process. A second experiment was conducted using a cathode with PVDF/HFP binder, which showed the best performance in the experiments presented in Fig. 2, achieving stable operation at 750 mA cm^{-2} (Fig. 2b and d). The experimental conditions were maintained identically as for the Nafion binder; however, the center compartment was initially flowed with deionized water (insertion of K_2SO_4 solution at t = 400 s). Initially, only very low current densities of 10–20 mA cm^{-2} were observed using deionized water (Fig. 3a, blue line). Upon feeding with 0.5 M K_2SO_4 solution, the current density steadily increased to more than 780 mA cm^{-2}. A PEIS experiment performed before and after the introduction of K_2SO_4 in the center compartment revealed a significant decrease in the low-frequency resistance R(1.258 Hz) from 29 Ω to 0.47 Ω (Fig. S3). This reduction aligns well with the increase of current density observed in the CA experiment shown in Fig. 3. Using a cathode with PVDF/HFP

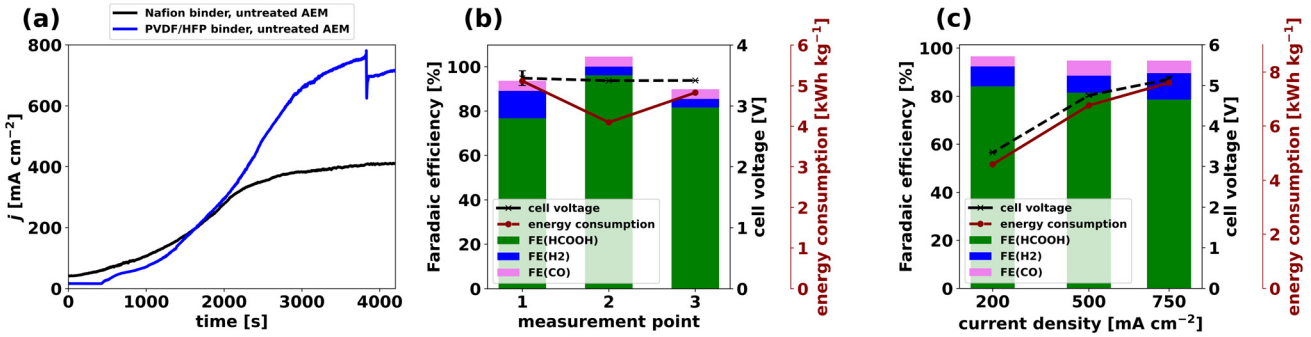

Fig. 3 (a) Initial cell activation using chronoamperometry at 5 V and continuous flow of 0.5 M K_2SO_4 solution in the center compartment (cc) at 0.1 mL min^{-1} using a cathode with a Nafion binder (black line) and PVDF/HFP (blue line; injection of 0.5 M K_2SO_4 solution in the center compartment starts at t = 400 s). (b) Faradaic efficiencies and energy consumption using a cathode with PVDF/HFP binder after cell activation using chronopotentiometry at 200 mA cm^{-2} over 3 h measuring time (1 h interval). (c) Chronopotentiometry at variable current density (sampling after 30 min of stable cell operation). Note: CO_2 flow in the cell activation was set to 150 sccm (a) and kept at a constant lambda (60–225 sccm) in the CP experiments (b–c). Liquid flows were maintained at 3 mL min^{-1} in the anode and 0.1 mL min^{-1} in the center compartment, using only deionized water in the CP experiments.

binder and the activation procedure shown in Fig. 3a, chronopotentiometry experiments were conducted at 200 mA cm^{-2} for 3 h (Fig. 3b), as well as under variable current density 200–750 mA cm^{-2} (Fig. 3c). Faradaic efficiencies and energy consumption showed improvements compared to results in Fig. 2, where cell activation by CA at 5 V was performed using a pre-treated PiperION AEM, and a one-time injection of 0.5 M K_2SO_4 solution before CA (2–3 mL over 20 seconds; see Experimental section).

From these experiments, we observed that pre-treating the AEM does not appear to be critical for achieving stable and efficient operation of the DFAP electrolyzer. However, activation with K^+ is essential for optimal performance in the eCO_2R process. Given the system's sensitivity to the activation method, maintaining a consistent activation protocol is strongly recommended to ensure the reproducibility of results.

Examining the long-term stability at high current densities

To investigate the stability of the catalyst over a longer time frame using the PVDF/HFP ionomer, CP experiments at 200 and 500 mA cm^{-2} were performed for 24 hours (Fig. 4). The activation of the cell proceeded as explained previously (an unactivated PiperION AEM was used, and a flow of 0.1 mL min^{-1} containing 0.5 M K_2SO_4 was fed during the ramp-up phase at 5 V). The data collection was started after initial equilibration at 200 and 500 mA cm^{-2}. Operating at 500 mA cm^{-2}, FE_{FA} oscillated around 70%, cell voltages below 5 V, and specific energy consumptions around 8 kWh kg^{-1} (Fig. 4a). During the 24 h of the cell operation at 200 mA cm^{-2}, FE_{FA} values remained around 75%, cell voltages fluctuated around 3.6 V, and specific energy consumption was approximately 5.7 kWh kg^{-1} (Fig. 4b). The results obtained in these experiments are comparable to those obtained in the short-time experiments (Fig. 2). The performance indicators in the 24 h time interval do not provide any sign of catalyst degradation.

In the 500 mA cm^{-2} experiment, the potassium content was analyzed in the eluent from the center compartment (cc) to

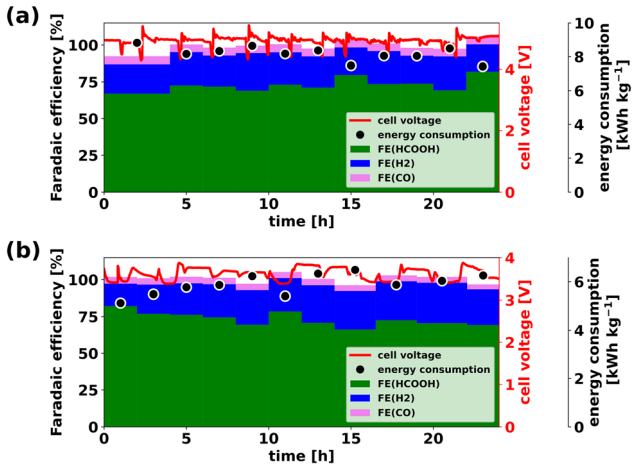

Fig. 4 Faradaic efficiency, cell voltage, and specific energy consumption *versus* time during 24 h operation of the DFAP electrolyzer, taking liquid samples every two hours. (a) Operation at 500 mA cm^{-2} and 150 sccm of CO_2 feed. (b) Operation at 200 mA cm^{-2} and 60 sccm of CO_2 feed. Tables S3 and S4 report detailed performance values.

evaluate potential diffusion of potassium from the catalyst layer to the center compartment, across the AEM. The liquid flow was collected at 2 h time intervals and analyzed using ICP-MS (Agilent 7900 ICP-MS). The potassium concentration was highest in the first sample (after 4 h), reaching 2.83 mg L^{-1}. In subsequent samples (2 h sampling), the potassium content ranged between less than 0.3 and 1.5 mg L^{-1} (Table S3). Considering the 0.1 mL min^{-1} flow in the center compartment and the average potassium concentration of 1.4 mg L^{-1}, the total amount of potassium diffusion to the center compartment during the 24 h experiment, given the collection of ~235 mL of eluent, is ~0.3 mg. This minimal loss of potassium does not seem to affect the observed cell voltages and selectivity of the catalyst, as observed in Fig. 4a.

Study of morphological changes on cathodic GDEs

To assess the degree of structural changes after electrolysis, top and cross-sectional view images of pristine and used GDEs (post-mortem) were recorded using Scanning Electron Microscopy (SEM). Energy Dispersive X-ray Spectroscopy (EDS) provided the elemental mapping of elements (C, Bi, O, F, and K). Fig. 5 displays SEM and EDS images of a cathodic GDE containing PVDF/HFP binder used in the eCO_2R experiment in Fig. 2. A cross-section SEM image of the pristine electrode before electrolysis presents a homogeneous distribution of the Bi_2O_3 catalyst characterized by its white color in the ~90 μm thick catalyst layer supported on the carbon fibers of the GDL (Fig. 5a). A cross-section SEM image of this GDE after electrolysis (Fig. 5b) reveals a fading of the white color in the ~25 μm of the catalyst layer annexed to the PiperION AEM, corresponding to a depletion of the catalyst content as confirmed by EDS mapping (lack of Bi and O content in this section, Fig. 5c). F and K content, stemming from the PVDF/HFP and K_2SO_4 cell activation, respectively, remain homogeneous through the catalyst layer (Fig. 5c and S4). Since the cell operates exclusively with deionized water during the CP experiments, the only source of potassium to the cell is the 0.5 M K_2SO_4 introduced in the center compartment during the activation step before CP. This confirms the ability of potassium ions to migrate across the AEM toward the cathode under the influence of the applied electric potential. Top-view SEM images at low magnification of the electrode (Fig. 5d) display circular indentations (∅ = 300–500 μm) caused by the mechanical compression of the ion exchange resin beads present in the center compartment. Surprisingly, the SEM image of the GDE surface reveals only isolated accumulations of catalyst, appearing as white regions (Fig. 5d). A higher magnification SEM image of the white region (Fig. S5a) shows flake-shaped crystals containing high amounts of C, O, and Bi, as confirmed by EDS analysis (Fig. S5b). The absence of catalytic material on the GDE surface (Fig. 5d) could result from mechanical detachment that occurred during the separation from the PiperION AEM. These observations indicate a migration of the catalytic material from the inner catalyst layers (~25 μm) and accumulation on the interface with the PiperION membrane as flake-shaped crystals with a high content of C, O, and Bi. This crystalline product may correspond to $Bi_2O_2CO_3$, as previously reported by other authors when Bi_2O_3 reacts with CO_2 in the presence of water.[29] In contrast, GDEs incorporating anionic binders (PiperION and Sustainion) exhibit a homogeneous distribution across the catalyst layer after electrolysis, whereas Nafion-containing GDEs also displayed depletion (Fig. S6). To gain deeper insight into the catalyst migration phenomenon observed with the PVDF/HFP binder, XCT measurements were performed. This technique enables the visualization of the three-dimensional distribution of the catalyst within the GDE and provides post-mortem information on the PiperION AEM, which is electronically non-conductive and can therefore not readily be imaged *via* SEM imaging.

X-ray computed tomography analysis

XCT imaging of the post-mortem cathode GDE using PVDF/HFP binder (Fig. 6, same sample as in the SEM image shown in Fig. 5b) confirms that approximately the top 25 μm of the ~60 μm-thick post-operation catalyst layer is devoid of the catalyst species (Fig. 6a). In contrast, the inner layers display high X-ray absorption, a result of the higher atomic number of bismuth. Faded white areas observed up to 0.4 mm within the GDL indicate the presence of low concentrations of catalyst embedded between the carbon fibers. XCT examination of the PiperION AEM reveals the presence of catalyst material on the membrane surface that was in contact with the GDE (Fig. 6b). This observation supports our hypothesis of catalyst migration from the initial inner layers (~25 μm) toward the GDE/AEM interface. Please note that the visible metal artifacts—bright and dark streaks—are caused by intentionally low X-ray energy settings, which were used to enhance the contrast of the membrane material. This image serves only to show the placement of the catalyst relative to the membrane surface and was not intended for quantitative analysis. The absence of a visible catalyst layer on the GDE in the SEM image (Fig. 5d) is attributed to the strong adhesion of the catalyst layer to the AEM. Upon disassembly, the AEM and the adhering catalyst (Fig. 6b)

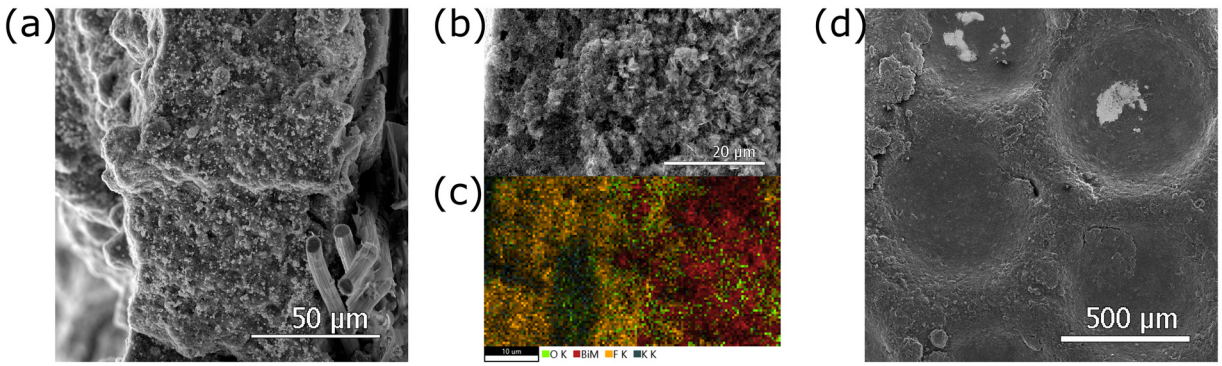

Fig. 5 Cross-section-view SEM images of a cathode electrode with PVDF/HFP binder in (a) pristine state before and (b) after eCO_2R. (c) EDS mapping content of the electrode in (b). Color code: Bi (red), O (green), F (yellow), K (grey), and C (not depicted). (d) Top-view SEM image at low magnification of the electrode in (b).

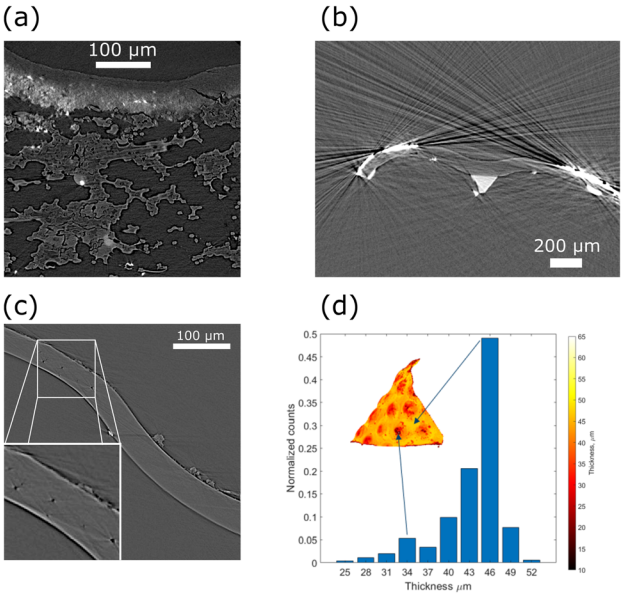

Fig. 6 Micro-XCT side-viewed images of post-mortem: (a) cathodic GDE with PVDF/HFP, (b) PiperION AEM after eCO_2R, and (c) PiperION AEM sample from (b), shown after mechanical surface cleaning. (d) Thickness map and histogram corresponding to a 3D image of the PiperION AEM used in (b).

detach from the GDE. A faded-white triangular area is also observable on the lower side of the AEM, attributed to residual $KHCO_3$ from sample preparation. Concavities on the AEM are consistent with indentations caused by the ion exchange beads from the center compartment, which are also visible in the SEM images of the GDE (Fig. 5d). To enable XCT characterization of the AEM's internal structure, mechanical surface cleaning was applied to remove highly absorbing bismuth-based material and residual $KHCO_3$ before the measurement shown in Fig. 6c. The inset (bottom-left corner) presents a magnified view displaying circular voids with darker contrast, a few micrometers in size, suspected to result from CO_2 gas evolution. This is attributed to HCO_3^-/CO_3^{2-} flux across the AEM and their reaction with a locally decreasing pH environment, indicating the presence of a pH gradient within the AEM, as previously reported.[15] Thickness mapping of the XCT data (Fig. 6d, see SI for the algorithm) reveals that the AEM is thinner at the indented positions. This is likely caused by mechanical strain during cell assembly and is expected to influence catalyst activity and selectivity due to the thickness-dependent function of the AEM as a proton barrier.[15] This observation may explain the different results observed in the eCO_2R using a cathode with PVDF/HFP, using two different cell activation procedures. In the results of Fig. 2, the AEM was pre-treated with KOH and assembled in its hydrated form. In contrast, for the results shown in Fig. 3b–c, the AEM was assembled untreated and in the dry state, requiring a longer activation period using a K_2SO_4 solution (see '*influence of cell activation*' for details). The use of a dry, untreated AEM likely results in less deformation caused by the ion exchange resin and contributes to the enhanced activity observed in this study (Fig. 3b–c). Our study suggests that assembling the PiperION AEM in the dry state, followed by *in situ* activation with K_2SO_4, may enhance eCO_2R (as illustrated in Fig. 3). However, further investigations are required to fully confirm and understand this hypothesis.

The role of potassium ions in the catalyst layer

The good performance at high current densities and low cell potential observed with the DFAP electrolyzer using the PVDF/HFP binder indicates the necessity of a catalyst layer (CL) with adequate conductivity, establishing ionic contact between the catalyst and the PiperION AEM. The initial activation of the cell using K_2SO_4 in the center compartment and the water flow across the PiperION membrane supplies sufficient water and potassium to achieve adequate aqueous electrolyte wetting of the cathodic catalyst layer, which is necessary to sustain the observed high current densities. This active catalyst layer should contain an aqueous electrolyte film to establish ionic contact between the catalyst and the AEM. The presence of an aqueous medium also aids in explaining the restructuring of the spherical Bi_2O_3 particles into the active catalyst sheets observed post-mortem.

The presence of potassium, as confirmed *via* EDS (Fig. S4a), plays a pivotal role in enabling ion conduction within this film, as deionized water alone is a poor ionic conductor (55 nS cm^{-1}). In the presence of CO_2, the formation of carbonic acid increases the conductivity only marginally to about 1 µS cm^{-1} at 25 °C,[30] whereas potassium-based electrolytes are commonly employed for their significantly higher ionic conductivity. To assess the influence of electrolyte conductivity in the CL of the DFAP electrolyzer, we calculated the maximum current density j corresponding to a given Ohmic loss ΔU across the catalyst layer (eqn (4), see SI for the derivation of the equation). This simple model assumes maximum activity of the catalyst near the AEM, which is reachable at a given maximum Ohmic loss and yields an upper limit for the current density one may expect, assuming a homogeneous, uninterrupted electrolyte film, whereas nonconductive gas and solid volumes are found inside the real CL. In the equation, ρ denotes the specific resistance, $i_{0,\text{apparent}}$ the limiting apparent catalyst activity (using the reported value of 583.9 A g^{-1} for the highly active Bi sheet catalyst in a DFAP electrolyzer),[16] $m_{Bi_2O_3}$ the catalyst load (fixed to 4 mg cm^{-1} for a 5 cm^2 active surface GDE), and d_{layer} the thickness of the catalyst layer (fixed to 60 µm).

$$j(\Delta U) = \begin{cases} \sqrt{\dfrac{2 i_{0,\text{apparent}} \cdot m_{Bi_2O_3}}{\rho \cdot d_{\text{layer}}} \cdot \Delta U}, j(\Delta U) < j_{\max} \\ j_{\max} = i_{0,\text{apparent}} \cdot m_{Bi_2O_3} \end{cases} \quad (4)$$

Fig. 7 displays the relationship between the achievable current densities j and the ohmic loss across the catalyst layer ΔU for different electrolytes. The conductivity of deionized water limits the current densities to below the 10 mA cm^{-2} mark, whereas a 10 wt% K_2CO_3 solution enables current densities up to

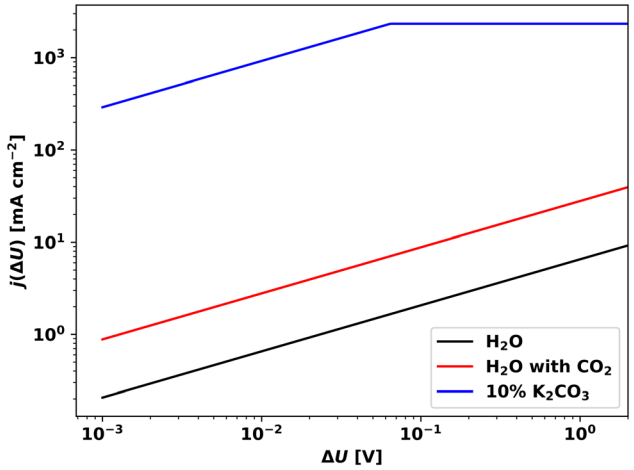

Fig. 7 Plot of the estimated upper achievable current density at specified Ohmic losses according to eqn (4) using the specific resistivity of deionized water (18 MΩ cm),[30] carbonic acid (1 MΩ cm),[30] and 10 wt% potassium carbonate solution (9.2 Ω cm).[31]

750 mA cm^{-2} with only tens of millivolts of ohmic overpotential. The model underestimates the actual cathodic ohmic resistance because it neglects the nonconductive gas and solid phases. Beyond enhancing electrolyte conductivity, alkaline metal ions play an essential role in CO_2 electroreduction by suppressing the HER and locally increasing the pH near the catalyst sites, thereby promoting eCO_2R selectivity.[22,32]

Causes of the observed catalyst displacement

The observed redistribution of catalyst material from the upper catalyst layers (~25 μm) toward the AEM—resulting in catalyst depletion within these layers (Fig. 5b–c) and accumulation at the CL|AEM interface—suggests a catalyst transport mechanism operating within the GDE. Cathodic corrosion of Bi(0) species through the formation of nascent BiH_3 and its subsequent decomposition in water[33–35] is unlikely to account for the long-range catalyst redistribution observed by XCT (Fig. 6a). Instead, bismuth dissolution, transport, and reprecipitation provide a more plausible explanation. Gaseous CO_2 in the CL is increasingly depleted toward the AEM due to its electrochemical conversion to formate and its chemical reaction with electrochemically generated hydroxide, forming bicarbonate and carbonate, which leads to a locally more alkaline environment near the AEM. Under wet conditions, Bi_2O_3 can partially dissolve into mobile hydroxo-containing complexes and subsequently reprecipitate as the alkalinity increases, particularly near the CL|AEM interface (see SI for a more detailed description).[36] The AEM positioned between the center and cathodic compartments acts as a barrier, leading to the accumulation of the Bi(0) and $Bi_2O_2CO_3$ species at the CL/AEM interface and catalyst depletion of the inner layers. Accumulation of Bi_2O_3-based catalysts at the CL surface has also been reported in flow cells without an AEM when using alkaline catholyte.[37]

The authors also proposed a dissolution/reduction cycle of the bismuth species that is driven by a pH gradient. Higher alkalinity is observed at the cathode|AEM interface, where the catalyst accumulation occurs (see SI for a detailed explanation). The observed catalyst migration in this work points to a self-optimization mechanism rather than a degradation process. Operation over 24 h at 200 and 500 mA cm^{-2} (Fig. 4), maintaining stable selectivity, potential, and energy consumption, is indicative of the stability of the created catalyst layer during this period. This catalyst migration, identified in post-mortem analysis after 3 h (Fig. 5c and 6a), appears to be beneficial, reducing ohmic losses by shortening the ion migration distance inside the catalyst layer. Furthermore, enhanced interfacial contact between the catalyst layer and the AEM was observed, with the catalyst layer remaining on the AEM rather than the MPL upon disassembly.

Techno-economic studies for industrial viability

A techno-economic analysis (TEA) assessed the viability of the DFAP electrolyzer to economies of scale. The analysis used optimal experimental results obtained in this study at 500 mA cm^{-2} (Fig. 2) using a Bi_2O_3-cathode with PVDF/HFP binder with a PiperION AEM (70% FE, 4.5 V, 7.46 kWh kg^{-1}, and 3.7 M formic acid). The economic performance was evaluated using the levelized cost of formic acid (LCFA) as a metric, based on an industrial-scale formic acid production, as modeled in our previous study.[21] This considers a DFAP reactor composed of 30 stacks of 200 cells with an active surface area of 0.6 m^2, accounting for a total reactor area of 3600 m^2. The TEA evaluates a process design incorporating the CO_2 electrolysis unit, a system for separating and recycling unreacted CO_2, and a distillation unit assumed to achieve a commercial formic acid concentration between 85 and 90 wt% using the baseline assumptions listed in Table S5. Fig. 8a presents a waterfall breakdown of the LCFA, totaling $0.567 per kg$_{FA}$. Within this value, the contribution associated with the DFAP electrolyzer reactor, CO_2 supply and recycling, product purification, reactor maintenance, and other operation expenditures (OpEx) amounts to $0.213 per kg$_{FA}$, while the energy component specific to the electrolytic process contributes to $0.354 per kg$_{FA}$ (62% of the LCFA).

The cost of energy of the electrolytic process is the most influential factor affecting economic performance. Therefore, accessing renewable energy sources at costs lower than the 4.5 cents per kWh assumed in the analysis, or reducing the energy consumption of the electrolysis, would enhance the economic viability of the process. To better understand the dependence of the LCFA on various operational parameters, a single-parameter sensitivity analysis was conducted and displayed in Fig. 8b. To interpret the sensitivity analysis (Fig. 8b), improved and worsened parameter values relative to those considered in the case base were calculated, while keeping all other parameters constant (Table S5), showing their influence on the LCFA. For example, using energy sources as cheap as 2.5 cents per kWh reduces the LCFA to $0.394 per kg$_{FA}$, compared with the original $0.567 per kg$_{FA}$ calculated using the 4.5 cents per kWh assumption (Fig. 8b).

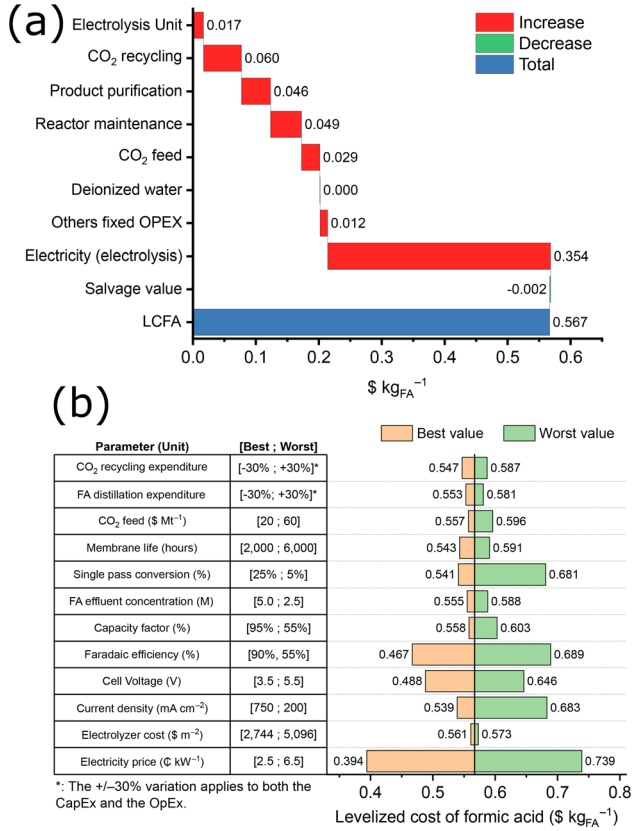

Fig. 8 (a) Waterfall breakdown of the levelized cost of formic acid (LCFA) obtained with our experimental data at 500 mA cm^{-2}, and (b) sensitivity analysis of the LCFA obtained in (a). Baseline electrochemistry parameters originate from the optimal experimental results using a Bi_2O_3-cathode with PVDF/HFP binder with a PiperION AEM (Table S1) and operating assumptions of Table S5.

TEA studies incorporating our experimental results from the DFAP electrolyzer into our previously reported model show a promising economic outlook with a LCFA of \$0.567 per kg_{FA}, surpassing the earlier reported value of \$0.69 per kg_{FA}.[21] This improvement is attributed to the higher formic acid concentrations achieved at relatively high current densities, which substantially reduce the downstream purification process. Consequently, the electricity cost for the electrolytic process (Fig. 8a) remains the most critical factor, showing a strong dependency in the sensitivity analysis (Fig. 8b) to energy price and the electrochemical parameters that influence energy consumption, such as faradaic efficiency and cell voltage.

Conclusions

In summary, we studied the influence of the binder used in custom-made Bi_2O_3-based GDEs on the performance of a DFAP reactor configured with a Nafion CEM and a PiperION AEM. Anionic (Sustainion), cationic (Nafion), and non-ionic (PVDF/HFP) polymers were used as binders in the custom-made cathodic GDEs. Contrary to expectations, anionic binders showed poor performance at higher current densities (350–500 mA cm^{-2}), even when the PiperION binder matched the PiperION AEM,[15] suggesting that a homogeneous GDE/AEM interface may be less critical than previously thought. The best performance of the DFAP electrolyzer was obtained with the non-ionic PVDF/HFP binder, delivering the highest reported current density to date (750 mA cm^{-2}) along with high faradaic efficiency (69%), enhanced formic acid concentrations (3.8 M; ~16 wt%), and an optimized energy consumption of 8.3 kWh kg^{-1}. The highest performance with the PVDF/HFP binder may lie in its higher hydrophobicity, which suppresses water accumulation within the catalyst layer, thereby enhancing CO_2 diffusion and supporting higher current densities. The initial K^+-based activation of the cell is also crucial for operation at higher current densities, as it promotes the formation of an *in situ* electrolyte film at the cathode, providing the ionic conductivity necessary to sustain these elevated current densities. SEM and XCT experiments of the post-mortem GDE revealed catalyst displacement from the initial inner layers (~25 μm) toward the GDE/AEM interface, likely caused by bismuth dissolution, transport, and subsequent reprecipitation. The TEA results demonstrate strong scalability potential based on the experimental data presented in this study, due to the ability to produce high concentrations of formic acid at high current densities.

Author contributions

SS, HT, BR, and RE conceived the idea. KvF collected and analyzed the data. KvF and SS interpreted the data. UN performed techno-economic analyses. KD conducted and analyzed XCT experiments. BS designed the analytical workflows. All authors contributed to the writing and editing of the manuscript.

Conflicts of interest

There are no conflicts of interest to declare.

Data availability

The data supporting this article have been included as part of the supplementary information (SI). Supplementary information is available. See DOI: https://doi.org/10.1039/d5gc06974b.

All data will be available in the future at https://data.fz-juelich.de.

Acknowledgements

We thank the financial support from the German Federal Ministry of Research, Technology, and Space (BMFTR) within the project 'iNEW2.0—Inkubator Nachhaltige Elektrochemische Wertschöpfungsketten' Project No. 03SF0627A and 'PHOENIX—Launch Space Power-to-X' Project No. 03SF0775A.

References

1 N. Li and A. Fratalocchi, *Global Challenge*, 2024, **8**, 2300306.
2 International Renewable Energy Agency IRENA, *Renewable power generation costs in 2020*, eBook Partnership, 2022.
3 M. Sterner and M. Specht, *Energies*, 2021, **14**, 6594.
4 B. Endrődi, E. Kecsenovity, A. Samu, T. Halmágyi, S. Rojas-Carbonell, L. Wang, Y. Yan and C. Janáky, *Energy Environ. Sci.*, 2020, **13**, 4098–4105.
5 I. Z. Montiel, A. Dutta, K. Kiran, A. Rieder, A. Iarchuk, S. Vesztergom, M. Mirolo, I. Martens, J. Drnec and P. Broekmann, *ACS Catal.*, 2022, **12**, 10872–10886.
6 M. O. Dauda, M. Bello, J. Hendershot, N. Kingsley, I. Agbadan, J. Park, S. Tasnim, O. Oduyebo, A. C. Engler, C. Plaisance and J. C. Flake, *ACS Appl. Energy Mater.*, 2025, **8**, 13607–13619.
7 C. W. Lee, J. S. Hong, K. D. Yang, K. Jin, J. H. Lee, H.-Y. Ahn, H. Seo, N.-E. Sung and K. T. Nam, *ACS Catal.*, 2018, **8**, 931–937.
8 Y. Guan, M. Liu, X. Rao, Y. Liu and J. Zhang, *J. Mater. Chem. A*, 2021, **9**, 13770–13803.
9 W. Zhang, Y. Hu, L. Ma, G. Zhu, Y. Wang, X. Xue, R. Chen, S. Yang and Z. Jin, *Adv. Sci.*, 2018, **5**, 1700275.
10 H. Yang, J. J. Kaczur, S. D. Sajjad and R. I. Masel, *ECS Trans.*, 2017, **77**, 1425.
11 M. Ramdin, A. R. T. Morrison, M. de Groen, R. van Haperen, R. de Kler, E. Irtem, A. T. Laitinen, L. J. P. van den Broeke, T. Breugelmans, J. P. M. Trusler, W. de Jong and T. J. H. Vlugt, *Ind. Eng. Chem. Res.*, 2019, **58**, 22718–22740.
12 J. M. Spurgeon and B. Kumar, *Energy Environ. Sci.*, 2018, **11**, 1536–1551.
13 H. Yang, J. J. Kaczur, S. D. Sajjad and R. I. Masel, *J. CO_2 Util.*, 2017, **20**, 208–217.
14 B. A. Rosen, A. Salehi-Khojin, M. R. Thorson, W. Zhu, D. T. Whipple, P. J. A. Kenis and R. I. Masel, *Science*, 2011, **334**, 643–644.
15 B. Rutjens, K. von Foerster, B. Schmid, H. Weinrich, S. Sanz, H. Tempel and R.-A. Eichel, *Ind. Eng. Chem. Res.*, 2024, **63**, 3986–3996.
16 C. Xia, P. Zhu, Q. Jiang, Y. Pan, W. Liang, E. Stavitski, H. N. Alshareef and H. Wang, *Nat. Energy*, 2019, **4**, 776–785.
17 L. Li, Z. Liu, X. Yu and M. Zhong, *Angew. Chem.*, 2023, **135**, e202300226.
18 L. Fan, C. Xia, P. Zhu, Y. Lu and H. Wang, *Nat. Commun.*, 2020, **11**, 3633.
19 H. Yang, J. J. Kaczur, S. D. Sajjad and R. I. Masel, *J. CO_2 Util.*, 2020, **42**, 101349.
20 K. Fernández-Caso, G. Díaz-Sainz, M. Alvarez-Guerra and A. Irabien, *ACS Energy Lett.*, 2023, **8**, 1992–2024.
21 U. Nzotcha, S. Sanz, H. Tempel and R.-A. Eichel, *Angew. Chem., Int. Ed.*, 2025, **64**, e202418114.
22 L.-P. Chi, Z.-Z. Niu, Y.-C. Zhang, X.-L. Zhang, J. Liao, Z.-Z. Wu, P.-C. Yu, M.-H. Fan, K.-B. Tang and M.-R. Gao, *Proc. Natl. Acad. Sci. U. S. A.*, 2023, **120**, e2312876120.
23 M. Großeheide, D. Schaffeld, R. Keller and M. Wessling, *Electrochem. Commun.*, 2023, **150**, 107487.
24 M. N. Idros, Y. Wu, T. Duignan, M. Li, H. Cartmill, I. Maglaya, T. Burdyny, G. Wang and T. E. Rufford, *ACS Appl. Mater. Interfaces*, 2023, **15**(45), 52461–52472.
25 T. H. M. Pham, J. Zhang, M. Li, T.-H. Shen, Y. Ko, V. Tileli, W. Luo and A. Züttel, *Adv. Energy Mater.*, 2022, **12**, 2103663.
26 M. Bass, A. Berman, A. Singh, O. Konovalov and V. Freger, *J. Phys. Chem. B*, 2010, **114**, 3784–3790.
27 X. Zhong, H.-J. Peng, C. Xia and X. Liu, *J. Phys. Chem. C*, 2024, **128**, 3621–3631.
28 X. Qin, H. A. Hansen, K. Honkala and M. M. Melander, *Nat. Commun.*, 2023, **14**, 7607.
29 J. Zeng, N. B. D. Monti, T. Chen, M. Castellino, W. Ju, M. A. O. Lourenço, P. Jagdale and C. F. Pirri, *Catal. Today*, 2024, **437**, 114743.
30 I. M. Ageev and Yu. M. Rybin, *Meas. Tech.*, 2020, **62**, 923–927.
31 *CRC Handbook of chemistry and physics*, ed. R. C. Weast, CRC Pr, Boca Raton, Fla, 70 edn, 1989.
32 M. C. O. Monteiro, F. Dattila, B. Hagedoorn, R. García-Muelas, N. López and M. T. M. Koper, *Nat. Catal.*, 2021, **4**, 654–662.
33 P. Deng, H. Wang, R. Qi, J. Zhu, S. Chen, F. Yang, L. Zhou, K. Qi, H. Liu and B. Y. Xia, *ACS Catal.*, 2020, **10**, 743–750.
34 D. S. Lee, *Anal. Chem.*, 1982, **54**, 1682–1686.
35 X. Chen, S. Chen, W. Huang, J. Zheng and Z. Li, *Electrochim. Acta*, 2009, **54**, 7370–7373.
36 E. V. Shkol'nikov, *Russ. J. Appl. Chem.*, 2010, **83**, 2121–2127.
37 F. Bienen, A. Löwe, J. Hildebrand, S. Hertle, D. Schonvogel, D. Kopljar, N. Wagner, E. Klemm and K. A. Friedrich, *J. Energy Chem.*, 2021, **62**, 367–376.